Optimum Receiver Location for Ultra Wideband In-Body Communication Based on Channel Capacity Calculation

Jan-Christoph Brumm
jan.brumm@tuhh.de

Gerhard Bauch
bauch@tuhh.de

Hamburg University of Technology
Institute of Communications
21073 Hamburg, Germany

ABSTRACT

For the design of ultra wideband (UWB) in-body communication links, e.g. for capsule endoscopes, it is vital to know which maximum data rates are achievable. The channel capacity gives a tool to quantify this theoretic limit. Calculating the channel capacity in a frequency dependent environment requires the knowledge of the transfer function of the communication channel. For this reason, a new channel modeling approach based on a multi-layered dielectric approximation of the human body is presented. From this model, the transfer functions for in-body communication are derived. Based on the channel capacity, we then investigate the number of receive antennas required for reliable high data rate transmission and where to place the receivers on the abdominal surface for optimum reception. Results show that one antenna is not sufficient for in-body UWB communication. However, if the number of antennas is increased to five, the 10 %-outage channel capacity can be increased up to 1.55 Gbit/s.

CCS Concepts

•Networks → Wireless personal area networks; Network performance modeling; •Mathematics of computing → *Information theory;*

Keywords

In-body, channel modeling, ultra wideband, channel capacity, receiver diversity

1. INTRODUCTION

Capsule endoscopes are a popular application for wireless in-body communication as they provide an alternative for classical endoscopy. However, for the capsule endoscopy to work, a lot of images have to be transmitted from a small device with limited energy reservoir. Most implants available today use the Medical Implant Communication Service Band (MICS) from 402 MHz to 405 MHz [8]. However, due to restrictions on the allowed bandwidth (300 kHz) only a data rate of up to 455.4 kbit/s is standardized [7].

To allow for better and more confident diagnoses by the physician, higher resolution images are required. Today's capsule endoscopes use images of at most 320×320 pixels [8]. Increasing the size of the images requires higher data rates. If the bandwidth is kept constant, a higher data rate requires a higher modulation order. To achieve the same bit error rate with a higher modulation order, the transmit power needs to be increased. However, if the bandwidth is increased as well, the data rate can be increased without having to increase the transmit power. For this reason ultra wideband is very attractive for high data rate transmission in in-body communication although the attenuation is much higher for higher frequencies.

Ultra wideband communication is allowed in the range of 3.1 GHz to 10.6 GHz whereas narrowband communication standards for in-body communication use frequencies up to 2.4 GHz. For UWB communication an equivalent isotropically radiated power spectral density of -41.3 dBm/MHz is allowed as maximum [3]. Furthermore, much smaller and simpler transmitter can be build for ultra wideband technology compared to narrowband communication [10].

To develop reliable communication links a good channel model is needed to simulate the data transmission. Channel models for in-body UWB propagation in the abdominal region have been published in literature, e.g. in [11][12][14]. However, in none of them the channel capacity has been investigated. In most of the published studies finite-difference time-domain (FDTD) simulations were carried out to gain insight into the propagation behavior. Additionally, experimental studies were carried out in [1] and [4]. Most of the studies resulted in path loss models only. However, for the calculation of the channel capacity in a frequency dependent medium like the human body an impulse response or transfer function model is needed. The authors in [12] developed a statistical impulse response model. Unfortunately, this has some plausibility problems.

For this reason, a new channel modeling approach is presented in the following. The idea is to model the transmission of the electromagnetic wave inside the human body with the help of a multi-layered dielectric. This simplification has the advantage that results can be calculated analytically with results from transmission line theory. With this approach, scattering at tissue boundaries inside the body is neglected. In [13] the basic idea of this approach is presented

BODYNETS 2016, December 15-16, Turin, Italy

DOI 10.4108/eai.15-12-2016.2267630

and formulas for the transfer function of a plane electromagnetic wave passing through a multi-layered dielectric are derived. These formulas are then validated with experiments and show that the analytically calculated path loss coincides well with the experimental results.

In this paper the idea from [13] is extended. Using the formulas from [13] the transfer functions for multiple possible transmitter and receiver locations inside the body and on the body surface are calculated. From these transfer functions the channel capacity will be computed. Using the statistical distribution of the channel capacity, given a certain distance between transmitter and receiver, the optimum receiver locations for multiple antennas are determined. Multiple antennas are combined using a selection diversity scheme. The selection diversity scheme selects always the antenna with the highest received signal power as the receiving antenna.

An important simplification, besides the fact that only plane wave propagation is considered, is that antenna effects are not included in our calculations. However, as the channel capacity gives an upper bound on the data rate, these simplifications will still lead to an upper bound. Moreover, comparison to other path loss models available in literature shows that the difference in path loss is acceptable, as will be shown later in this work.

The remaining paper is structured as follows. In Section 2 the channel modeling approach is described in detail and formulas for the channel capacity are derived. Section 3 compares our proposed channel model to already existing path loss models and power delay profiles to validate the results. Furthermore, in Section 4 the optimum receiver locations for different number of antennas are presented together with the achievable channel capacity. Section 5 concludes the paper.

2. CHANNEL MODELING SETUP AND CAPACITY CALCULATION

2.1 Prerequisites and Assumptions

For the development of a channel model for in-body communication, a model of the human body is needed. In this paper the Visible Human body model provided by the Helmholtz Zentrum München is used [6]. The provided model consists of a 3D matrix indicating the position of the different human tissues inside the body. Each voxel element in this matrix has a resolution of $0.91\,\text{mm} \times 0.94\,\text{mm} \times 5\,\text{mm}$ in (x, y, z) direction. Figure 1 shows one slice in the (x, y)-plane and the view from the right side onto the body.

To calculate transfer functions for the in-body communication channel, the following setup was used. At first 7405 possible transmitter locations inside the gastrointestinal tract have been randomly selected, such that the distance between each location is at least 4 mm. For each of these possible transmitter locations the tissue composition (thickness and type) is investigated along a straight line in the (x, y)-plane. In total 100 directions were analyzed per transmitter location, as indicated in Figure 1a for two examples. Thus, it is assumed for simplicity reasons that a receiver is always positioned at the same height z on the body surface as the transmitter inside the body. In total 740 500 communication links were investigated in terms of their tissue composition.

The tissue composition is then interpreted as a multi-layered dielectric consisting of the found tissue types. This

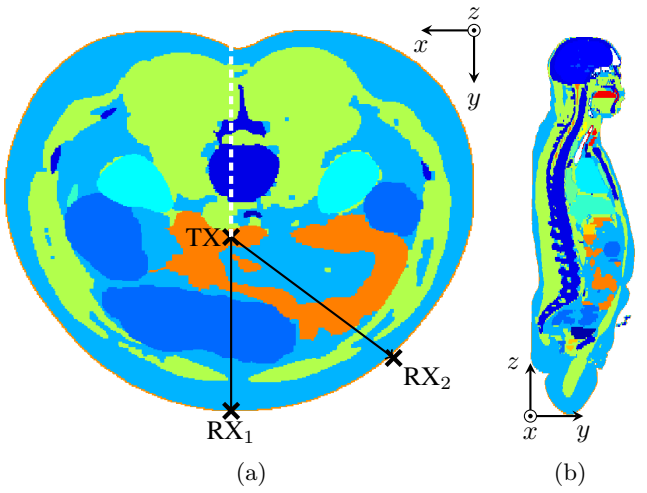

Figure 1: Visible Human voxel model. (a) View of one slice in the (x, y)-plane from top. (b) View from the right side. The ●-colored area is the small intestine and the ●-colored area is the colon. Two possible receiver locations are marked with RX and one possible transmitter location is marked with TX. The tissues along the dashed white line are used for the source impedance calculation of the link from TX to RX_1.

setup can be seen in Figure 2. In the following sections, the formulas to determine the transfer function of a plane electromagnetic wave traveling through a multi-layered dielectric are derived.

2.2 Dielectric Properties of Human Tissue

The tissue in the human body is essentially a frequency dependent lossy dielectric. Investigations from Gabriel *et al.* showed that the frequency dependent behavior of the relative permittivity can be modeled by the following Cole-Cole expression [5]:

$$\varepsilon_r(f) = \varepsilon_\infty + \sum_{n=1}^{4} \frac{\Delta\varepsilon_n}{1 + (j2\pi f\tau_n)^{1-\alpha_n}} + \frac{\sigma}{j2\pi f\varepsilon_0}, \quad (1)$$

where ε_∞ is the permittivity for $f \to \infty$, σ is the conductivity, ε_0 is the permittivity of free-space, f is the frequency, and $\Delta\varepsilon_n$, τ_n, α_n are tissue specific parameters. Details on the parameters can be found in [5]. The relative permeability of human tissue is assumed to be $\mu_r = 1$.

2.3 Transfer Function of a Multi-Layered Dielectric

The propagation of a plane wave through a multi-layered dielectric, as depicted in Figure 2, can be described by the transmission matrix $\mathbf{T}$ of the dielectric. The matrix $\mathbf{T}$ gives the relationship between the electric and the magnetic fields at the boundary i to the fields at the boundary $i + 1$

$$\begin{bmatrix} E_i \\ H_i \end{bmatrix} = \mathbf{T}_i \begin{bmatrix} E_{i+1} \\ H_{i+1} \end{bmatrix}. \quad (2)$$

For each layer i the transmission matrix $\mathbf{T}_i$ is defined as [13]

$$\mathbf{T}_i = \begin{bmatrix} A_i & B_i \\ C_i & D_i \end{bmatrix} = \begin{bmatrix} \cosh\gamma_i d_i & \eta_i \sinh\gamma_i d_i \\ \frac{1}{\eta_i}\sinh\gamma_i d_i & \cosh\gamma_i d_i \end{bmatrix}, \quad (3)$$

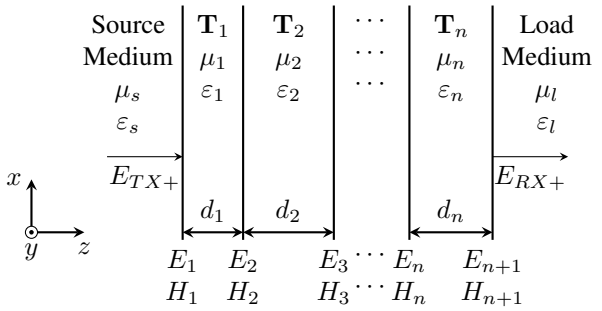

Figure 2: A plane wave E_{TX+} propagating through a multi-layered dielectric. The wave propagates along the positive z-direction.

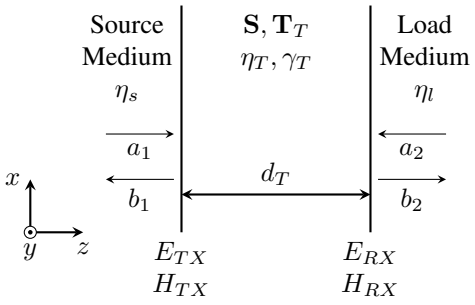

Figure 3: Equivalent dielectric of the total tissue composition for the computation of the S-parameters.

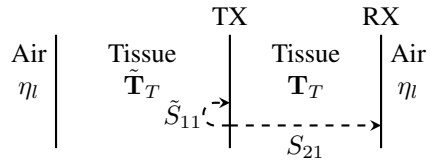

Figure 4: Calculation of the source impedance is based on the reflection coefficient $\tilde{S}_{11}$ at the transmitter.

where $\gamma_i = j2\pi f\sqrt{\mu_i\varepsilon_i}$ is the propagation constant, $\eta_i = \sqrt{\mu_i/\varepsilon_i}$ is the wave impedance and d_i is the thickness of the i-th medium. With these definitions the total composition of all n dielectrics can be described by $\mathbf{T}_T = \mathbf{T}_1 \cdot \mathbf{T}_2 \cdots \mathbf{T}_n$.

To calculate the transfer function $H_{CH}(f) = \frac{E_{RX+}}{E_{TX+}}$, a conversion of the **T**-matrix into its scattering (**S**-) parameters is needed. Note that the source and load impedances are not real. For this scenario Theilmann *et al.* derived the necessary conversion formulas in [13]. For a better understanding the derivation is summarized here. Refer to [13] for more details.

The matrix $\mathbf{T}_T$ is now converted into its **S**-parameter representation with power parameters $a_1, a_2, b_1,$ and b_2 as shown in Figure 3. The power parameters are defined as [13]:

$$a_1 = \sqrt{\Re(\eta_s)}H_{TX+} \qquad b_1 = \sqrt{\Re(\eta_s)}H_{TX-} \tag{4}$$

$$a_2 = \sqrt{\Re(\eta_l)}H_{RX-} \qquad b_2 = \sqrt{\Re(\eta_l)}H_{RX+}\,, \tag{5}$$

where η_s and η_l are the wave impedances of the source and load medium, respectively. The electric and magnetic field at the boundaries to the source and load medium have been split into a forward and a backward traveling wave $E_{TX} = E_{TX+} + E_{TX-}$ and $H_{TX} = H_{TX+} - H_{TX-}$, likewise for E_{RX} and H_{RX}. The subscripted + indicates a wave traveling in positive z-direction and a − indicates a wave traveling in negative z-direction. Moreover, the following relationship of electric and magnetic field of a plane wave holds[1]:

$$E_{TX+} = \eta_s H_{TX+} \qquad E_{TX-} = \eta_s H_{TX-} \tag{6}$$

$$E_{RX+} = \eta_l H_{RX+} \qquad E_{RX-} = \eta_l H_{RX-}\,. \tag{7}$$

Taking (4) to (7) the power parameters are defined in such a way that the squared magnitude of the scattering parameters give the ratio of incoming to outgoing power for each medium. The path loss is then

$$|S_{21}|^2 = \left|\frac{b_2}{a_1}\,|_{a_2=0}\right|^2 = \frac{\frac{1}{2}\Re(\eta_s)\,|E_{RX+}|^2}{\frac{1}{2}\Re(\eta_l)\,|E_{TX+}|^2} = \frac{P_{RX+}}{P_{TX+}}\,, \tag{8}$$

where P_{TX+} is the time average power transmitted inside the dielectric from the source medium and P_{RX+} is the power received by a receiver inside the load medium. With these definitions, S_{21} can be expressed in terms of the entries of the $\mathbf{T}_T$-matrix as

$$S_{21} = \frac{\sqrt{\Re(\eta_l)}}{\sqrt{\Re(\eta_s)}}\frac{2\eta_s}{\eta_l A_T + B_T + \eta_l\eta_s C_T + \eta_s D_T}. \tag{9}$$

Combining (9) with (8), the channel transfer function $H_{CH}(f)$ can be derived in terms of S_{21} as

$$\begin{aligned} H_{CH}(f) = \frac{E_{RX+}}{E_{TX+}} &= \frac{\eta_l\sqrt{\Re(\eta_s)}}{\eta_s\sqrt{\Re(\eta_l)}} \cdot S_{21} \\ &= \frac{2\eta_l}{\eta_l A_T + B_T + \eta_l\eta_s C_T + \eta_s D_T}. \end{aligned} \tag{10}$$

As the source and load impedance are complex in this case, it has to be noted that in general $S_{21} \neq S_{12}$. This does not influence the electromagnetic reciprocity, only **S** is not necessarily symmetric [9].

2.4 Source and Load Impedance

The receiver is placed on the body surface, that means the wave impedance of the load medium is always set to the wave impedance of air $\eta_l = 376.73\,\Omega$. However, the transmitter is placed somewhere in the gastrointestinal tract and, thus, there are reflections occurring from parts of the wave that propagate away from the receiver. These reflection effects will be included in the source impedance. Consider the example depicted in Figure 1a. The tissue through which the wave passes on its way to the receiver lies along the black arrow connecting TX and RX_1. To include the reflections occurring at the transmitter, the tissues in the opposite of this direction are considered (indicated by the dashed white line in Figure 1a). This idealized setup is shown in Figure 4. The tissue composition along the opposite direction of the communication signal is denoted by the matrix $\tilde{\mathbf{T}}_T$. With this, the source impedance can be calculated from the

[1]Note: the conjugate complex that occurs at this point in [13] in equation (A2) should in our opinion not appear here.

reflection coefficient $\tilde{S}_{11}$ as [13]

$$\eta_s = \frac{\eta_l \tilde{A}_T + \tilde{B}_T}{\eta_l \tilde{C}_T + \tilde{D}_T}\,. \tag{11}$$

Where η_l is the impedance of air and $\tilde{A}_T, \tilde{B}_T, \tilde{C}_T$, and $\tilde{D}_T$ are the components of $\tilde{\mathbf{T}}_T$.

2.5 Channel Capacity in Frequency-Selective AWGN Channels

The channel capacity gives an upper limit on the data rate that may be transmitted over a communication channel. As long as the data rate is smaller than the capacity, there exist error correcting codes which theoretically enable communication with an arbitrarily low error rate. However, if the data rate is greater than the capacity, there exist no such codes.

For a real channel with additive white Gaussian noise limited to the frequency band B the channel capacity in bit/s can be calculated as [2]:

$$C = B \log_2\left(1 + \frac{P_{TX+}}{N}\right) = B \log_2\left(1 + \frac{2 \cdot E_s}{N_0}\right). \tag{12}$$

Where P_{TX+} is the transmit power, N is the noise power, $E_s = \frac{P_{TX+}}{2B}$ the energy per transmit symbol, and $\frac{N_0}{2}$ the two-sided noise power spectral density.

In a frequency-selective channel the capacity can be defined for a small subband Δf around a center frequency f_i. If the channel transfer function $H_{CH}(f)$, the power spectral density of the transmit signal $S_{XX}(f)$, and the power spectral density of the noise $S_{NN}(f)$ are assumed to be constant in this subband, the resulting channel capacity is [2]

$$C(f_i) = \Delta f \log_2\left(1 + \frac{2 \cdot S_{XX}(f_i)\,|H_{CH}(f_i)|^2}{S_{NN}(f_i)}\right). \tag{13}$$

For $\Delta f \to 0$ the total capacity C of the channel yields

$$C = \int_0^\infty \log_2\left(1 + \frac{2 \cdot S_{XX}(f)\,|H_{CH}(f)|^2}{S_{NN}(f)}\right) \mathrm{d}f. \tag{14}$$

As an AWGN channel is assumed, the noise power spectral density is $S_{NN} = \frac{N_0}{2} = \frac{kT}{2} = -156.93\,\mathrm{dBm/Hz}$ ($T = 20\,^\circ\mathrm{C}$ and an additional 20 dB noise figure in the receiver).

3. COMPARISON TO EXISTING CHANNEL MODELS

To classify our results, the following section compares the presented model to other models available in literature. The comparison is limited to those studies which also investigate the propagation behavior in the abdominal region for ultra wideband transmission.

3.1 Path Loss Comparison

For better comparability we split the different available path loss models into two groups. The first resides in the frequency band of 1 GHz to 6 GHz and the second from 3.4 GHz to 4.8 GHz.

3.1.1 Path Loss for 1 GHz to 6 GHz

In [12] Støa *et al.* simulated a plane wave with the finite-difference time-domain (FDTD) method. This plane wave, excited by a Gaussian pulse, was sent onto the body surface.

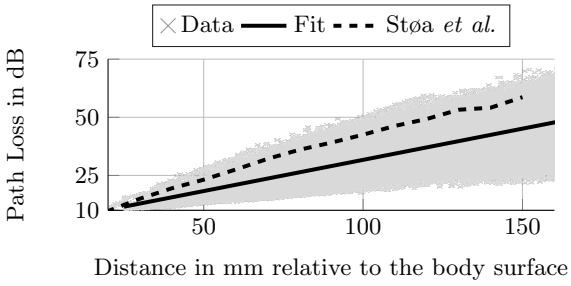

Figure 5: The path loss model from Støa *et al.* [12] compared to the data and the exponential fit determined from our proposed model. In both cases the transmission bandwidth was 1 GHz to 6 GHz.

The pulse had most of its energy in the frequency range of 1 GHz to 6 GHz. Their resulting path loss model is calculated from the received power inside the abdomen with several hundred ideal electric and magnetic field probes. Thus, their model excludes any antenna effects. However, as they did a FDTD simulation, scattering of the signal inside the body is included. The average path loss from the simulation in [12] is shown in Figure 5 with the dashed line.

In our proposed model antenna effects are excluded as well. However, also scattering inside the body is not taken into consideration, that means on average a lower path loss is expected. In Figure 5 the path loss of all the 740 500 communication links is depicted with gray crosses. This path loss was calculated from (9) in the range of 1 GHz to 6 GHz. An exponential fit through that data gives the average path loss, which can be expressed in dB as

$$P_{\mathrm{dB}} = P_0 + \alpha \cdot d\,, \tag{15}$$

where $P_0 = 4.86\,\mathrm{dB}$, $\alpha = 0.268\,\mathrm{dB/mm}$ and d is the distance between transmitter and receiver in the interval from 21 mm to 335 mm. The average path loss is shown in Figure 5 with the solid black line. It can be seen that, as expected, the average path loss of the proposed model is smaller. However, the model from Støa *et al.* still lies inside the data range of our model.

3.1.2 Path Loss for 3.4 GHz to 4.8 GHz

For this frequency range three paper were found. Their path loss models are compared in Figure 6. Shi *et al.* did a FDTD simulation including transmit and receive antenna in the range of 3.4 GHz to 4.8 GHz. Thus, scattering inside the body was considered. Experimental results are reported in [4] from Floor *et al.* Using an anesthetized pig the authors measured the path loss with a vector network analyzer in the frequency range of 1 GHz to 6 GHz. Figure 6 shows the curve for 4 GHz. The two curves from Floor *et al.* and Shi *et al.* show a very similar behavior. However, the result from Thotahewa *et al.* does not fit to them. In [14] Thotahewa *et al.* did a FDTD simulation in the frequency range 3.5 GHz to 4.5 GHz also including antenna effects. Nevertheless, the results from Thotahewa *et al.* are approximately 10 dB above the results from the other two papers. The reason might be that different antennas were used.

The results from our model are again plotted with gray crosses and an exponential fit approximates the average path loss very good. The parameters for (15) are in this case

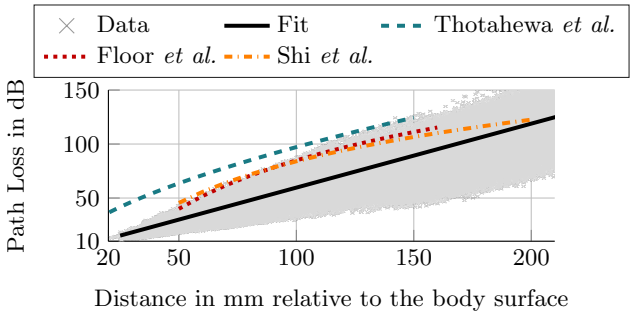

Figure 6: The path loss models from Thotahewa *et al.* [14], Floor *et al.* [4], and Shi *et al.* [11] compared with the data and exponential fit from our proposed model for a frequency range of 3.4 GHz to 4.8 GHz.

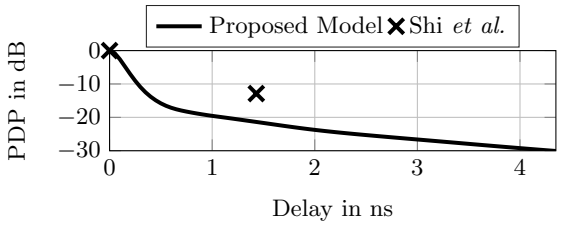

Figure 7: Power delay profile of the model from Shi *et al.* [11] and of the proposed model shown in dB relative to the first path.

$P_0 = 0.401\,\text{dB}$ and $\alpha = 0.592\,\text{dB/mm}$. The resulting curve is shown as a solid black line in Figure 6.

As in Figure 5, it can be seen from Figure 6 that all models from literature estimate a higher path loss than our model, due to the scattering inside the body that is included. Another fact that can be observed is that the shape of the curves is different whether antenna effects were included or not. All path loss models without any antenna effects have a more linear behavior in dB. Those models including antenna effects have a more logarithmic behavior.

3.2 Power Delay Profile Comparison

A common way to compare the channel models of multi-path propagation environments is the power delay profile. It is a measure of how the received power is spread in time. Of all the available channel models only the one of Shi *et al.* [11] lead to a reproducible power delay profile. In Figure 7 the power delay profile from Shi *et al.* is compared to the resulting power delay profile of our proposed model. The resulting RMS delay spread is $\tau_{\text{RMS}} = 0.58\,\text{ns}$ for our model and for the model from Shi *et al.* $\tau_{\text{RMS}} = 0.31\,\text{ns}$. Additionally, the difference between the two models at a delay of $\tau = 1.43\,\text{ns}$ is only 8 dB. Hence, the multi-path characteristics of the two models are very similar.

4. CHOICE OF THE OPTIMUM RECEIVER LOCATION

For the calculation of the channel capacity a transmission bandwidth of 3.1 GHz to 4.8 GHz was considered; this is the so-called UWB low band which is preferable due to its lower attenuation [11]. The transmit power was set to

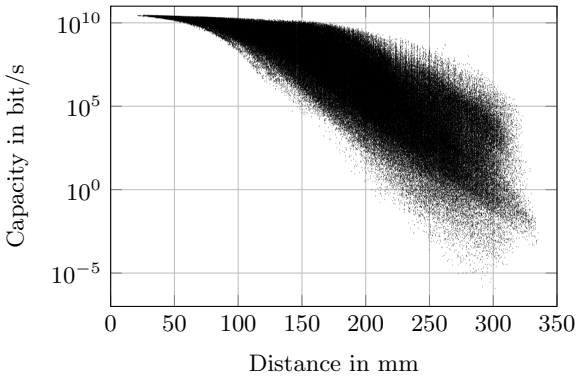

Figure 8: Scatter plot of the channel capacity over the distance between tansmitter and receiver.

21.5 mW and distributed equally in the transmission band. Simulations in [14] revealed that this is the maximum transmit power that can be used without violating the specific absorption rate limits set by the International Commission on Non-Ionizing Radiation Protection.

4.1 Distance Dependency of the Channel Capacity

The channel capacity is calculated using (10) and (14) for each of the 740 500 communication links. In Figure 8 every dot represents the channel capacity of one communication link plotted against the distance between transmitter and receiver. It can be seen that as the distance increases the scattering of the channel capacity is increasing drastically. At a distance of 250 mm for example the channel capacity varies between 10^{-3} bit/s and 10^{7} bit/s. Starting from approximately 320 mm the capacity drops drastically. The largest distance occurring in the simulation is 335 mm.

Based on this capacity distribution the optimum position of the receive antennas is calculated. The distance d between transmitter and receiver is discretized in steps of 1 mm. From all capacity values that fall into one of these distance bins the probability distribution of the channel capacity C given a certain distance d $f_C(C|d)$ is calculated.

For the plot in Figure 8 it was assumed that the receiver is always placed on the same height as the transmitter. This was done to simplify the simulation and reduce the number of possible communication links to simulate. As the composition of the human body is highly heterogeneous, it should on average not make a significant difference if the signal is transmitted a certain distance in a strictly horizontal direction or the same distance in any inclined direction. For this reason the probability distribution $f_C(C|d)$ will be used as a model to calculate the channel capacity based on the distance d between any point on the body surface and a point in the gastrointestinal tract.

4.2 Optimum Receiver Location Based on the Maximum 10 %-Outage Channel Capacity

To determine the optimum receiver location, the abdominal surface was discretized in 181 patches, which were investigated as possible receive antenna location (these are the non-white patches in Figure 9). In Figure 9 the 10 %-outage capacity is shown for one antenna placed at each of the dis-

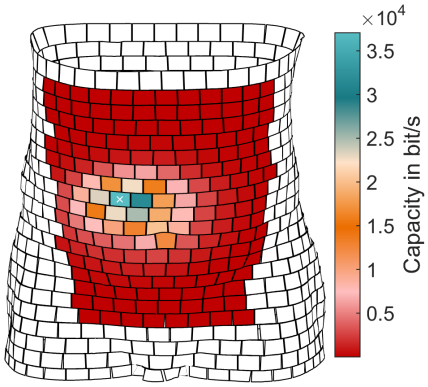

Figure 9: Distribution of the 10 %-outage capacity on the abdominal surface for one receive antenna. The optimum location is marked with a white X.

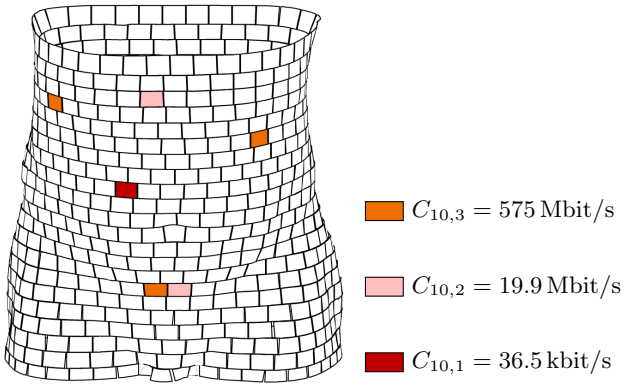

Figure 10: Optimum position in terms of maximum 10 %-outage channel capacity of up to three receive antennas operating in a selection diversity scheme.

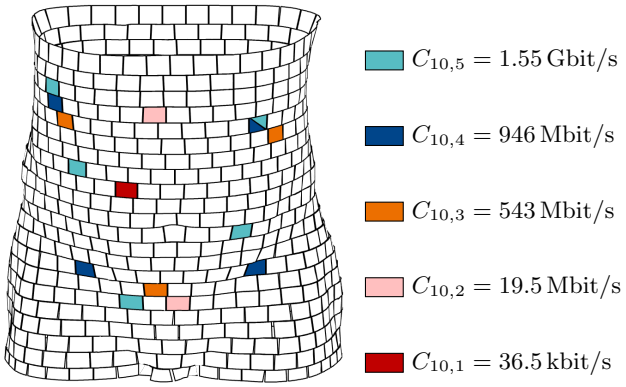

Figure 11: Optimum position determined based on the minimum 90$^{\text{th}}$ percentile of the distance of up to five receive antennas operating in a selection diversity scheme.

crete patches. For each patch i in Figure 9 the distances to all 7405 transmitter locations inside the body were determined, rounded to the nearest mm and stored in the vector $\mathbf{d}_i$. Distances larger than 335 mm were mapped to a distance of 335 mm as higher distances are not present in our model.

The probability distribution of the capacity $f_C(C|d)$ was then used to draw 100 samples of the capacity for each distance in $\mathbf{d}_i$. Finally, the statistical distribution of all capacity samples was used to calculate the 10 %-outage capacity. The 10 %-outage capacity is the capacity value which is achieved at least in 90 % of all realizations. Thus, it gives an indication of the reliability of the connection under the present channel conditions.

It can clearly be seen that there is only one area slightly above the navel where the capacity is greater than 5×10^3 bit/s. The location marked with the white X is the optimum position where a 10 %-outage capacity of 3.6×10^4 bit/s can be achieved.

Comparing this resulting capacity with the data rates specified for communication in MICS band in IEEE 802.15.6 [7] of 455.4 kbit/s it is clear that using only one antenna is not sufficient to improve the data rate.

Thus, it was investigated how the usage of multiple antennas can improve the channel capacity. The antennas were assumed to operate in a selection diversity scheme. Selection diversity is a non-optimal receiver diversity scheme in which the strongest received signal is selected. The diversity gain with other techniques as maximum-ratio combining might be higher, but this scheme requires more complex simulation and is out of the scope of this paper.

The approach to find the optimum position of multiple receive antennas on the abdominal surface is the same as for one antenna. However, the capacity samples are drawn for each receiver location separately. The samples are then compared for each realization and for each the maximum is picked. This resembles the selection diversity scheme, as the highest available channel capacity is related to the channel with the highest SNR. From this resulting vector of samples the 10 %-outage capacity is calculated. This calculation was repeated for all possible combinations of locations until the maximum was found.

In Figure 10 the results for one, two and three receive antennas are shown. For two antennas the locations indicated by the light red patches are optimum and yield a total 10 %-outage channel capacity of 19.9 Mbit/s. This is an improvement of nearly three orders of magnitude compared to one receive antenna. However, increasing the number of antennas to three does not lead to another increase in capacity of that amount. The capacity is 575 Mbit/s for three receive antennas placed at the orange patches in Figure 10.

The result for three antennas already indicates that there is potential for a high data rate transmission using UWB for in-body communication. Nevertheless, we were interested in the effect of even more receive antennas. Unfortunately, the computation time for the calculation of the optimum position based on the channel capacity is very high. However, it was observed that using only the minimum distance as a criterion for the optimization showed results that were near the ones shown in Figure 10.

4.3 Optimum Receiver Location Based on the Minimum Distance

To compute the optimum receiver locations based on the minimum distance, the distance vectors $\mathbf{d}_i$ were computed for each of the involved possible receiver locations i. The distance vectors were then compared directly. It was assumed that the link with the shortest distance results in the high-

est channel capacity, although it can be seen from Figure 8 that this is not necessarily the case. Thus, a vector with the minimum distance from each position inside the body to a receiver on the body results. From this vector the 90^{th} percentile is computed. Hence, only 10 % of the communication links have a larger distance than this value. This value is computed for each possible combination of receiver locations on the body and from them the minimum is selected as the optimum.

For this optimum position the 10 %-outage capacity is calculated and shown in Figure 11. It can be seen that the optimum location for one antenna is the same as in Figure 10. For two and three antennas the optimum locations are slightly different by just one discrete patch. The resulting 10 %-outage channel capacity for these configurations is only slightly smaller than the results using optimization based on the channel capacity. Hence the optimum location for four and five antennas is calculated and indicated by the dark blue and light green patches in Figure 11, respectively. The resulting 10 %-outage capacity is 946 Mbit/s for four antennas and 1.55 Gbit/s for five antennas. These results show that the 10 %-outage capacity seems to increase by ≈ 500 Mbit/s per receive antenna that is added after the second antenna. However, this behavior has to saturate at some point, as the capacity cannot increase infinitely. For 181 antennas, each placed on one of the discrete patches, the 10 %-outage capacity converges to 10.2 Gbit/s. Due to time constraints it was not possible to evaluate more than five antennas. Thus, it is unclear for which number of receive antennas the saturation starts.

As can bee seen in Figure 11 it is for all numbers of antennas optimum to place the receive antennas in a circular shape around the navel. Moreover, it is important, if more than two antennas are positioned, to place one of the antennas in the upper most right corner of the abdominal surface for optimum reception.

5. CONCLUSION

In this paper a new approach for the modeling of ultra wideband in-body communication was presented. It is based on a multi-layered dielectric representation of each communication link. With this model the channel capacity can be calculated. A comparison to already existing path loss models showed that the difference in path loss is small, although antenna effects and scattering inside the body were neglected. Based on the probability density function of the channel capacity the optimum locations for one to three receive antennas, working in a selection diversity scheme, were determined. It has been shown that with three antennas in their optimum position a 10 %-outage channel capacity of 575 Mbit/s can be achieved. Furthermore, results for four and five antennas were computed based on the minimum of the 90^{th} percentile of the distance. For five receive antennas the 10 %-outage channel capacity is 1.55 Gbit/s. This shows that an increase in data rate, to support higher resolution images for capsule endoscopy, is achievable with ultra wideband technology as long as enough receive antennas are placed on the abdomen. Furthermore, it can be seen from the results that by adding more antennas the 10 %-outage channel capacity increases approximately linear with the number of antennas.

6. REFERENCES

[1] D. Anzai *et al.* Experimental Evaluation of Implant UWB-IR Transmission With Living Animal for Body Area Networks. *IEEE Transactions on Microwave Theory and Techniques*, 62(1):183–192, Januar 2014.

[2] J. R. Barry *et al. Digital Communication.* Springer, 3rd edition, 2004.

[3] Federal Communications Commission. Revision of Part 15 of the Commission's Rules Regarding Ultra-Wideband TransmissionSystems.

[4] P.-A. Floor *et al.* In-Body to On-Body Ultra Wideband Propagation Model Derived from Measurements in Living Animals. *IEEE Journal of Biomedical and Health Informatics*, 19(3):938–948, 2015.

[5] S. Gabriel *et al.* The dielectric properties of biological tissues: III. Parametric models for the dielectric spectrum of tissues. *Physics in Medicine and Biology*, 41(11):2271–2293, 1996.

[6] Helmholtz Zentrum München Deutsches Forschungszentrum für Gesundheit und Umwelt. Virtual human database, 2016. [Online]. Available: http://www.helmholtz-muenchen.de/amsd/service/scientific-services/virtual-human-database/index.html

[7] IEEE Std 802.15.6-2012, IEEE Standard for Local and metropolitan area networks - Part 15.6: Wireless Body Area Networks, 2012.

[8] A. Kiourti *et al.* Implantable and Ingestible Medical Devices with Wireless Telemetry Functionalities: A Review of Current Status and Challenges. *Bioelectromagnetics*, 35(1):1–15, 2014.

[9] R. B. Marks and D. F. Williams. A General Waveguide Circuit Theory. *Journal of Research of the National Institute of Standards and Technology*, 97(5):533–562, 1992.

[10] A. F. Molisch. Introduction to UWB Signals and Systems. In B. Allen *et al.* , editor, *Ultra-Wideband: Antennas and Propagation for Communications, Radar and Imaging*, pages 1–17. John Wiley & Sons, Ltd, Chichester, UK, 2006.

[11] J. Shi *et al.* Channel Modeling and Performance Analysis of Diversity Reception for Implant UWB Wireless Link. *IEICE TRANSACTIONS on Communications*, E95-B(10):3197–3205, 2012.

[12] S. Støa *et al.* An Ultra Wideband Communication Channel Model for the Human Abdominal Region. In *IEEE Globecom Workshops*, pages 246–250, 2010.

[13] P. Theilmann *et al.* Computationally Efficient Model for UWB Signal Attenuation Due to Propagation in Tissue for Biomedical Implants. *Progress In Electromagnetics Research B*, 38:1–22, 2012.

[14] K. M. S. Thotahewa *et al.* Propagation, Power Absorption, and Temperature Analysis of UWB Wireless Capsule Endoscopy Devices Operating in the Human Body. *IEEE Transactions on Microwave Theory and Techniques*, 63(11):3823–3833, 2015.